Journal of Materials Chemistry A

ROYAL SOCIETY OF CHEMISTRY

PAPER

View Article Online
View Journal

Cite this: DOI: 10.1039/d5ta10373h

Comparison of the Arrhenius parameters between conventional hydrothermal and microwave-assisted synthesis methods for tin oxide nanoparticles

Morgan Chen,[a] Laura Glei Graversen,[b] Sanjit Ghose,[c] Kirsten M. Ø. Jensen[b] and B. Reeja-Jayan*[a]

Microwave (MW) irradiation has emerged as a powerful tool for accelerating materials synthesis, yet the origins of its specific influence on reaction kinetics remain elusive. While multiple studies have attributed the observed enhancements in reaction rates under MW heating to reduced activation energies, other accounts have suggested modifications to the Arrhenius pre-exponential factor as the predominant cause. Distinguishing between these parameters in modern applications of MW processing in nanomaterials requires experimental approaches capable of resolving the dynamic and nuanced structural kinetics that govern MW-assisted chemistry. Here, we combine *in-situ* synchrotron X-ray total scattering with pair distribution function (PDF) analysis to track the structural evolution of SnO_2 nanoparticles synthesized *via* MW-assisted and conventional hydrothermal conditions. Avrami modeling and Arrhenius analysis suggest that although MW irradiation yields a higher apparent activation energy, the enhanced crystallization is better explained by a pre-exponential factor several orders of magnitude larger than that of conventional heating. These findings suggest that the MW field induces a higher frequency of successful molecular rearrangements rather than lowering the intrinsic activation barrier. The results contribute further insights clarifying the role of the applied MW field for materials design where MW-specific effects can be deliberately harnessed. Furthermore, this work presents a framework promoting the utility of *in-situ* PDF characterization coupled with kinetic analysis for developing more sophisticated descriptions of nanoscale transformations for MW-driven reaction kinetics.

Received 20th December 2025
Accepted 19th May 2026

DOI: 10.1039/d5ta10373h

rsc.li/materials-a

1 Introduction

The application of microwave (MW) radiation in materials processing has been topic of considerable scientific intrigue in recent decades. Since its initial inception within the domain of organic chemical synthesis, numerous studies involving MW-assisted processing of materials have demonstrated experimental effects that are not observed *via* conventional processing methods.[2] Although the literature is abundant with reports of enhanced reaction rates,[4–6] improved product yields or purity,[7,8] lower necessary synthesis temperatures,[9–11] or even atypical material properties of irradiated products,[12–14] the precise nature of the underlying interactions between the incident MW field and the reactant species remains elusive and speculative. While thermal phenomena specific to MW heating, such as volumetric or selective heating, are well established, the existence of particular nonthermal effects of the applied MW field remains a controversial topic.[1,15,16]

One reoccurring interpretation of the unique influence of MW irradiation in materials synthesis is that it lowers the activation energy of a reaction, providing an alternative reaction coordinate.[17,18] For instance, studies on the MW-assisted crystallization of various lead-based perovskite thin films demonstrated shorter reaction times and lower synthesis temperatures relative to conventional processes, and this was correlated with decreases in the activation energy of the MW-activated process by roughly 30–40% compared to that of conventional heating.[19,20] An investigation comparing the hydrogen-based reduction of magnetite under MW and conventional heating reported that MW heating halved the apparent activation energy of its conventional counterpart, resulting in a greater extent in the reduction and metallization of magnetite with MW irradiation.[21] Similar accounts of accelerated reaction kinetics in MW processing have been described with considerable diminutions in the apparent activation energy relative to conventional heating for a variety of other metal oxide systems.[22–24]

[a]Department of Mechanical Engineering, Carnegie Mellon University, Pittsburgh, PA 15213, USA. E-mail: bjayan@andrew.cmu.edu
[b]Department of Chemistry and Nano-Science Center, University of Copenhagen, 2100 Copenhagen Ø, Denmark
[c]National Synchrotron Light Source II, Brookhaven National Laboratory, Upton, NY 11973-5000, USA

However, a handful of studies have instead suggested that the Arrhenius pre-exponential factor may play a more decisive role in governing the distinct effects, such as the faster kinetics, of MW-assisted synthesis. For example, an early study investigated the synthesis of titanium carbide powder *via* the carbothermal reduction of titania.[25] Reaction rates were more than three times faster under MW heating than conventional heating, and this was attributed to a comparable increase in the calculated pre-exponential factor with no appreciable change in the activation energy. Another study systematically investigated the influence of various MW processing parameters on the synthesis of silicoaluminophosphates (SAPO) zeolite crystals.[26] They found that MW heating increased both the activation energy and pre-exponential factor of SAPO-11, with the pre-exponential factor being several magnitudes higher than that of conventional synthesis and more likely to explain the improved reaction rate. A similar finding was determined by monitoring changes in crystallinity from diffraction measurements for the synthesis of a metal–organic framework material *via* conventional electric heating, ultrasound irradiation, and MW heating.[27] Unsurprisingly, MW heating resulted in accelerated synthesis (two-to-threefold increase) over conventional heating; however, this was also associated with both increased pre-exponential factors and activation energies compared to that of conventional heating. Therefore, the increased rate of synthesis was attributed to the increased pre-exponential factor rather than commonly-cited decreased activation energies.

Further elucidating the role of the applied MW field requires time-resolved, atomically sensitive experimental probes that can resolve the dynamic and nuanced effects of MW-assisted synthesis.[1,3] Therefore, *in-situ* characterization methods are necessary to reveal the rapid phase transitions and reaction kinetics that aren't captured in *ex-situ* studies.[18,28] While *in-situ* diffraction studies have previously been performed to directly monitor phase transformations during MW processing,[29–31] the use of traditional X-ray diffraction (XRD) suffers from the inability to appropriately characterize nanoscale materials or structures with varying degrees of atomic disorder.[32,33] For such applications where crystallinity is compromised or features of interest reside on the nanoscale, as has been demonstrated in MW-synthesized materials,[8,10,13,30] total scattering and atomic pair distribution function (PDF) analysis provide a more suitable tool over conventional powder diffraction. With PDF analysis, structural resolution from the local to global order can be studied with a single probe, enabling characterization of the incipient precursor reaction species all the way to the final amorphous/crystalline product(s). However, integrating *in-situ* total scattering measurements with MW irradiation poses nontrivial experimental challenges and has represented a major bottleneck in uncovering the fundamental mechanisms underlying MW-assisted synthesis.

Recent *in-situ* PDF studies have successfully revealed crystallization pathways during MW-assisted synthesis and provided experimental evidence for local MW heating effects at the atomic level.[34–36] A prior study inspiring the one presented herein demonstrated enhanced crystallization of SnO_2 nanoparticles in MW-assisted synthesis relative to conventional hydrothermal synthesis.[6] The more rapid growth of larger crystallites was associated with distinct changes in the evolution of the local atomic structure and atomic oxygen displacement parameter that did not occur with conventional heating during the reactions. Despite these seminal findings, further work is necessary to clarify the nature of the role of the applied field in MW-assisted synthesis.

The aim of this study is to address these gaps by extracting the Arrhenius parameters in the synthesis of SnO_2 nanoparticles. Determining the apparent activation energies and pre-exponential factors yields quantitative information on the influences of the MW field on the reaction kinetics and intrinsic activation barriers. Such insights can consequently provide a clearer interpretation of the role of the applied field in promoting phase formation. We chose SnO_2 as our material system for a couple of key reasons. Firstly, a number of relevant studies for both conventional and MW-assisted hydrothermal synthesis of SnO_2 have established experimental precedence to provide a useful foundation for mechanistic comparison.[6,37] Furthermore, SnO_2 is a versatile and promising material for a wide array of electrochemical applications in gas sensors, optics, batteries, and catalysis.[38–40] We observe that MW-assisted synthesis of rutile SnO_2 nanoparticles demonstrates rapid crystallization relative to conventional hydrothermal synthesis. The structural evolution of the irradiated chemical precursor seems to increasingly deviate from that under conventional heating as the applied MW power increases, demonstrating that the extent of the MW effect is dependent on the intensity of MW exposure. By applying Avrami modelling with Arrhenius analysis, we show that the faster crystallization corresponds with an elevated apparent pre-exponential factor rather than a reduced apparent activation energy, suggesting that the applied MW field augments the frequency of successful molecular rearrangements rather than modifications to the intrinsic activation barrier. Resolving this knowledge gap remains a critical obstacle in harnessing the specific benefits of the MW field in realizing modern paradigms for ecological materials processing and precise materials design.

2 Methods

2.1 Synthetic procedures for tin oxide nanoparticles

Tin(IV) chloride pentahydrate ($SnCl_4 \cdot 5H_2O$, 98%) powder (Sigma-Aldrich, USA) was dissolved in deionized (DI) water to form a 2 M aqueous precursor solution. The solution was contained inside borosilicate tubes (Hilgenberg GmbH, Germany) with an outer diameter of 3 mm and a wall thickness of 0.3 mm. The reaction tubes were sealed with quick-setting epoxy (J-B Weld Company, USA) and an assembly of graphite ferrules (Trajan Scientific and Medical, USA) and steel cap fittings (Swagelok Company, USA). The reaction tubes were then inserted into the process chamber of a bespoke MW waveguide built for *in-situ* X-ray scattering experiments and designed in collaboration with Gerling Applied Engineering. A schematic diagram of the system is depicted in Fig. 1. A similar setup to the one used in the present study, including the MW system, has been previously described.[6]

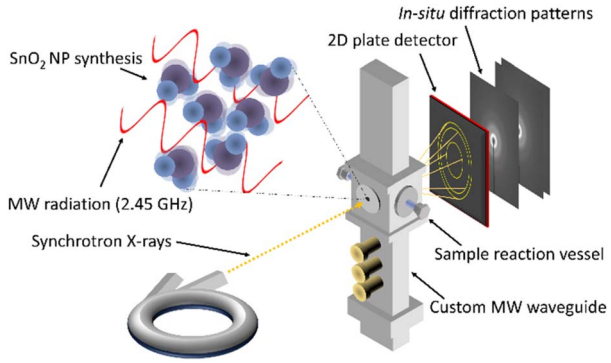

Fig. 1 Schematic diagram of the experimental setup involving *in situ* total scattering measurements with the custom MW reactor during nanoparticle synthesis. The precursor sample is loaded into a borosilicate vessel within the MW chamber. MW radiation at 2.45 GHz is supplied to the waveguide *via* a coaxial cable from a solid-state MW generator. The incident X-rays are directed into the inlet port of the MW chamber that contains the sample reaction vessel and are scattered onto a 2D area detector located behind the outlet port of the MW chamber throughout the chemical reaction.

The hydrothermal synthesis of SnO_2 nanoparticles was conducted *via* conventional and MW-assisted methods. The conventional synthesis method involved the application of a convective heat gun (Maxwel Manufacturing, Hong Kong) that was mounted adjacent to the MW process chamber and set to a desired output temperature spanning the range of 200–240 °C. The MW-assisted synthesis method was performed with mixed-heating involving the application of conventional heating and MW radiation. This was done to maintain a comparable heating rate to that of the conventional synthesis method to afford a more direct comparison with the results from conventional syntheses. This was necessary due to the inherently slower heating rate of the pulsed MW deposition scheme used to mitigate the pressure buildup in the 0.9 mL reaction vessel during the experiments. The MW-assisted synthesis method was achieved with the heat gun set to a constant output temperature of 100 °C and MW output powers spanning 20–40 W with an exposure cycle of 1 second on and 4 seconds off. An experimental reaction time of 35 minutes was set for all conditions. However, some of synthesis conditions were terminated prematurely during nanoparticle growth due to vessel implosion from autogenous pressure buildup.

The reaction temperatures for each of the experimental conditions were measured by adhering a fiber optic temperature probe (Qualitrol Corp, USA) to the surface of the reaction tube *via* a thermally conductive ceramic compound (Artic Silver, Inc., USA). For the synthesis experiments that reached steady state, the reaction temperatures (of the liquid solution) were measured to be 164 °C, 174 °C, and 181 °C under conventional hydrothermal synthesis conditions and 130 °C and 138 °C under MW-assisted synthesis conditions (Fig. S1). A maximum temperature of 143 °C was recorded for the final MW-assisted synthesis. Although this experiment did not reach an appreciable steady-state temperature, the results have been included for completeness and where applicable. Future references to the temperatures from the synthesis conditions will be that of the measured temperatures.

2.2 Pair distribution function (PDF) data acquisition and analysis

The *in situ* X-ray PDF experiments were conducted at the X-ray Powder Diffraction (XPD) 28-ID-2 beamline at the National Synchrotron Light Source II (NSLS-II) at Brookhaven National Laboratory (BNL). The MW system was installed at the hutch at beamline 28-ID-2. PDF data was collected according to the rapid acquisition PDF (RA-PDF) method.[41] A 2D PerkinElmer silicon image-plate detector (2048 × 2048 pixels with 200 × 200 μm pixel dimensions) was positioned 247.33 mm behind the sample. The incident wavelength of the synchrotron radiation was $\lambda = 0.182$ Å. Calibration measurements were done with CeO_2, and all datasets were collected at room temperature. The PDF data processing was performed using PDFgetX3 within the xPDFsuite software to subtract out the signal from the background and to set the Fourier transformation limits.[42,43] The data was transformed with $Q_{min} = 0.5$ Å^{-1} and $Q_{max} = 17.5$ Å^{-1} with $r_{poly} = 0.9$ Å. Structural refinements and analysis were conducted using PDFgui.[44] Refinements were conducted in the range of 1.5–50 Å and implemented Nyquist data sampling. The instrument resolution parameters Q_{damp} and Q_{broad} are refined when fitting the standard CeO_2 data, and are fixed in the subsequent structural refinements of PDF data, where $Q_{damp} = 0.0307$ Å^{-1} and $Q_{broad} = 0.0478$ Å^{-1}.[44,45] Experiments conducted with DI water at identical settings with regard to the experimental parameters for the conventional and MW-assisted synthesis conditions were performed to obtain the corresponding temperature-dependent background scattering signal. This component was subsequently subtracted from the total scattering signal for the respective dataset before analysis of the data. The data acquisition, reduction, and analysis are described in greater detail in the SI.

3 Results and discussion

3.1 Nanostructures in the synthesis of SnO_2 nanoparticles

A plot of the time-resolved PDFs describing the formation of rutile SnO_2 nanoparticles from the $SnCl_4$ precursor solution for a conventional hydrothermal synthesis experiment is shown in Fig. 2(a). Expectedly, there are no significant structural correlations beyond 5 Å at the beginning of the reaction, indicating a monomeric complex. Early nuclear magnetic resonance (NMR) spectroscopy studies revealed that aqueous solutions of $SnCl_4$ comprised of several species, such as $[SnCl_4(H_2O)_2]$ or $[SnCl_3(H_2O)_3]^+$, in various quantities.[46] To simplify its representation, an initial discrete model for $[SnCl_4(H_2O)_2]\cdot H_2O$ was used to approximate the amorphous precursor complexes.[37] During the refinements with this model, the H atom was removed due to its negligible scattering power. The crystal water was included in the model but was not independently refined due to its weak contributions to the PDF. A scale factor, low-r correlation parameter (δ_1), and isotropic atomic displacement parameters (U_{iso}) were refined to the experimental PDF data of the precursor solution as shown in Fig. 2(b). The spherical nanoparticle size parameter was set to 7 Å to only capture the nearest-neighbor distances for the Sn–O and Sn–Cl bonds, and

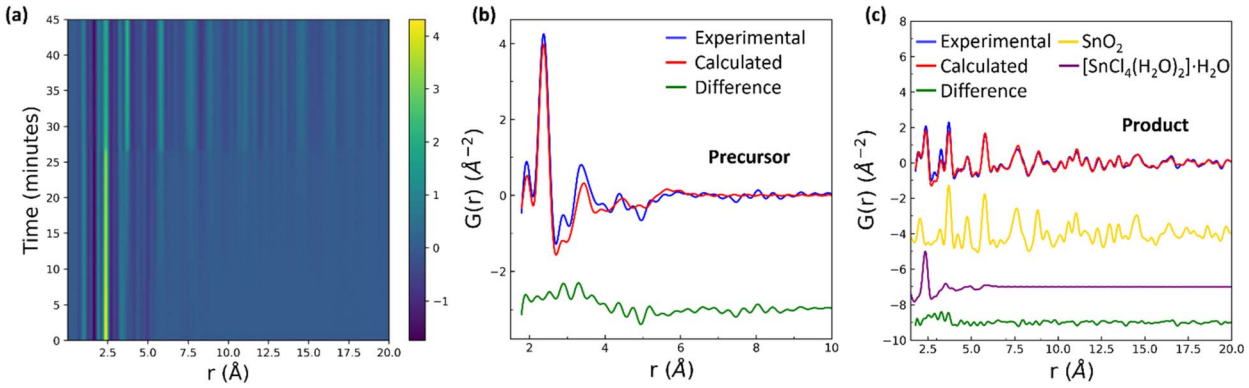

Fig. 2 Representative plots of the collected *in situ* PDFs and the resultant PDF refinements. (a) Time-resolved map of the *in situ* PDFs corresponding to the conventional hydrothermal synthesis of SnO_2 nanoparticles at 164 °C. (b) The PDF refinement of the precursor solution near the beginning of the synthesis reaction. The experimental data (blue) is fit to a $[SnCl_4(H_2O)_2]$-complex (red) with the difference offset below in green. (c) The PDF refinement of the final synthesized product near the end of the synthesis reaction. The experimental data (blue) is fit to a mixed-phase model (red) comprising the $[SnCl_4(H_2O)_2]$ complex and the crystalline rutile SnO_2 phase with the difference offset below in green. The calculated PDFs for the $[SnCl_4(H_2O)_2]$ (purple) and SnO_2 (yellow) phases are offset below.

symmetry constraints were automatically imposed on the atomic positions according to space group, $P2_1/c$. While some misfit exists, the overall fit is agreeable and illustrates that this simplified approach sufficiently describes the intensity ratios of the Sn–O and Sn–Cl bonds at *ca.* 2.17 Å and 2.37 Å, respectively. Furthermore, these experimental and refined peak locations are in good agreement with previous diffraction studies of *cis*-$[SnCl_4(H_2O)_2]$ which described Sn–O and Sn–Cl distances of 2.13–2.15 Å and 2.37–2.39 Å, respectively.[47]

The synthesis of SnO_2 nanoparticles yielded the crystalline rutile phase as shown in Fig. 2(c). A scale factor, the lattice parameters (a, c), a low-r correlation parameter (δ_1), isotropic atomic displacement parameters (U_{iso}), and a spherical nanoparticle size parameter were refined. Refinements of the evolution of the monomeric complexes in the precursor solution to the final crystalline rutile SnO_2 nanoparticles included both the $[SnCl_4(H_2O)_2]\cdot H_2O$ and SnO_2 phases in which the ratio of the constituent models was allowed to vary. The refined parameters are provided in Table S1. Similar modelling strategies have been implemented before.[6,37] The analytical workflow and general trends described here are also relevant to the total scattering data from the experiments performed at the other synthesis conditions (Fig. S2).

3.2 Formation of SnO_2 nanoparticles in conventional and MW-assisted syntheses

The final experimental PDFs from the conventional hydrothermal synthesis and MW-assisted synthesis methods are shown in Fig. 3. Specifically, the PDFs for all the synthesis conditions in the long-range order (LRO) domain are shown in Fig. 3(a). The extent of the PDF oscillations in the MW-synthesized samples is similar to that of the conventionally prepared SnO_2 nanoparticles, suggesting that the final spherical nanoparticle diameters from the MW method are comparable to those from the conventional method despite a deficit of more than 30 °C in their nominal reaction temperatures. The final diameters of the nanoparticles as determined by the PDF refinements from the conventional hydrothermal synthesis conditions at 164 °C, 174 °C, and 181 °C are 39 Å, 49 Å, and 45 Å, respectively, while the final spherical diameters of the nanoparticles synthesized *via* the MW-assisted method at 130 °C, 138 °C, 143 °C are 38 Å, 39 Å, and 41 Å, respectively (Table S1). The results seem to suggest that the resultant nanoparticle diameters at the present experimental conditions are not heavily dependent on the synthesis temperature. This observation is also supported by findings from previous studies involving the hydrothermal synthesis of rutile SnO_2 nanoparticles which reported that the particle size was not temperature dependent below 200 °C and seemed to stabilize around 4 nm.[37]

The formation of the crystalline rutile phase was consistent between the resultant SnO_2 nanoparticles from both synthesis methods with no significant deviations in the final lattice parameter values (Table S1). Similarly, the PDFs of the resultant products in the local range, corresponding to the local atomic arrangements, are comparable across the experimental conditions as shown in Fig. 3(b). Previous studies of MW-processed samples have demonstrated varying degrees of amorphization or disordering induced in the resultant atomic structure of the irradiated materials, especially those probing the local atomic environments *via* PDF characterization.[8,10,12,13,48] However, the PDFs of the final SnO_2 nanoparticles in the local domain seem largely comparable between the MW-assisted and conventional hydrothermal synthesis methods in the present experimental conditions. The PDF peaks at 3.8 Å and 5.7 Å are characteristic of the Sn–Sn bond in rutile SnO_2. The peak around 2.0 Å corresponds to Sn–O bonds present in the tin chloride precursor and final rutile phase while the peak at 2.4 Å corresponds to Sn–Cl interatomic distances. The persistent intensity of the Sn–Cl peak in the final PDF of the synthesized nanoparticles suggests that the formation of SnO_2 predominantly involves the coordination of concomitant Sn–O complexes to the precursor species rather than the chloride complexes

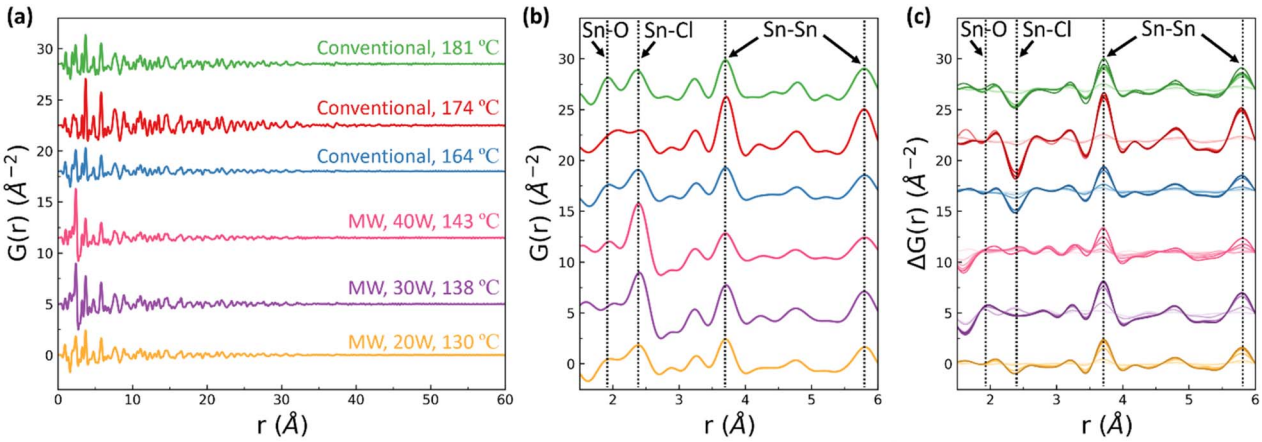

Fig. 3 PDF results of the synthesized SnO_2 nanoparticles. (a) The experimental PDFs of the final SnO_2 nanoparticles for the various synthesis conditions in the LRO. (b) The corresponding experimental PDFs of the final SnO_2 nanoparticles in the SRO. (c) The $\Delta G(r)$ plots for the various synthesis conditions in the SRO throughout their synthesis reactions. Lighter colors represent earlier reaction times while darker colors represent later reaction times.

themselves. This notion is supported by the considerable presence of the precursor complexes indicated by the resultant phase fractions from the refinements (Table S1) and has also been reported previously in comparable studies.[6,37] Overall, the similarity of the PDFs in the local domain suggests that the local atomic arrangements in the final synthesized SnO_2 nanoparticles were consistent between the synthesis methods.

To further evaluate structural differences between the synthesis methods, the difference PDF, $\Delta G(r)$, was applied to the *in-situ* PDFs to discern structural differences in the context of phase formation. The $\Delta G(r)$ is given by eqn (1):

$$\Delta G(r) = G(r) - G(r)_{t=0} \quad (1)$$

where $G(r)$ is any PDF following the start of the reaction, and $G(r)_{t=0}$ is the PDF at the start of the reaction at $t = 0$ corresponding to the initial precursor phase. Accordingly, positive peaks represent an emergence of interatomic bonds forming at that r value relative to the precursor tin chloride structure while negative peaks represent a loss of interatomic distances at that r value. *In-situ* characterization offers more transparent and representative insights into the dynamic nature of MW-induced structural effects that can be concealed by purely *ex-situ* measurements.

The $\Delta G(r)$ plots for the MW-assisted and conventional hydrothermal synthesis methods throughout their respective reaction durations are shown in Fig. 3(c). For both synthesis conditions, the development of peaks at the Sn–Sn bond lengths of 3.8 Å and 5.7 Å as the reaction progresses illustrates the formation of rutile SnO_2 as expected. Furthermore, the depressions around 2.4 Å corresponding to the Sn–Cl bond intensity signify that the tin chloride complexes were involved, representing a decrease in the Sn–Cl interatomic correlations during phase formation. These trends and the overall time-resolved profiles of the PDFs seem largely consistent among the conventional synthesis conditions and the MW-assisted synthesis at 130 °C. At an initial glance, this similarity contrasts with a previous MW study that observed noticeable differences in the nearest neighbouring distances in the $\Delta G(r)$ between MW-assisted and conventional hydrothermal syntheses of SnO_2 performed at 140 °C and 150 °C, respectively, thereby suggesting a mechanistic change under an external MW field during phase formation.[6] However, the MW conditions in the present experiment performed at 130 °C are less intense with regard to the exposure cycle and applied power, which could affect the extent of the physical or discernible influence of the external MW field on crystallization. Indeed, prior studies in MW-assisted chemistry have demonstrated that variations in the applied MW parameters affected the final properties of the irradiated specimens and the influence of the MW field's effect.[9,24,48,49] Furthermore, the concentration of the precursor solution in the present study (2 M) is different than that used in the aforementioned study (1 M), which would affect the scattering signal and derived PDFs. Nonetheless, further inspection shows that as the applied MW power increases from 20 W to higher levels at 30 W and 40 W, structural deviations illustrated by the $\Delta G(r)$ become more prominent and distinguished from that displayed by the conventional hydrothermal method. The existence of low intensity peaks in the r region from 2.5 Å to 2.9 Å that are not evident during conventional synthesis is also in excellent qualitative agreement with the results from former experiments.[6] While the assignment of specific interatomic distances in this range is nontrivial due to the potential overlap of Sn–Sn, O–O, and Sn–Cl peaks, the present study further illustrates the effect of the MW field in the evolving structural deviations in this region during the phase formation of SnO_2 at increasing applied MW powers.

3.3 Kinetics of SnO_2 nanoparticle formation in conventional and MW-assisted syntheses

The *in-situ* total scattering method allows further investigation into the kinetics of crystallization of the SnO_2 nanoparticles, providing an opportunity to survey fundamental differences in

kinetic properties, such as the apparent activation energies or rate constants, that can further clarify the role of the applied MW field. While *in-situ* X-ray diffraction (XRD) techniques are well-established for the quantitative analysis of reaction kinetics,[50–53] the use of the PDF method has further expanded quantitative studies of phase formation and crystallization kinetics into nanomaterials.[37,54,55] The Kolmogorov–Johnson–Mehl–Avrami model, also referred to as the Avrami model, has been widely applied to describe and study phase transformations for a variety of material systems.[28,55–58] While it was originally developed for solid-state reactions, its application has proven useful for studying the crystallization kinetics of various nanomaterials synthesized under hydro- and solvothermal conditions.[59–61] In such cases, the Avrami equation offers a straightforward, phenomenological framework for extracting kinetic parameters, such as apparent activation energies, or identifying relative trends in reaction behavior.[56] The formulation for representing Avrami behavior can be expressed by eqn (2):

$$\alpha = 1 - e^{-(kt)^n} \tag{2}$$

where α is the transformed fraction of the reactant to the product, k is the reaction rate constant, t is the reaction time, and n is the Avrami exponent reflecting the geometry of the transformation. The fraction of the transformed product can be estimated from the refined scale factors of the final rutile SnO_2 phase. The full curves for the transformation fractions representing the formation of the SnO_2 nanoparticles for the synthesis conditions are shown in Fig. 4. A portion of the red curve representing the conventional synthesis condition at 174 °C near the middle of the reaction time was redacted due to an experimental artifact resulting from particle agitation during data collection. Nonetheless, the shapes of the phase transformation curves largely exhibited the traditional sigmoidal profiles characteristic of the Avrami model. The phase transformation curves further support the observation that MW exposure improved the synthesis of the SnO_2 nanoparticles, resulting in comparable or even higher crystallization rates at lower measured temperatures than that of the conventional hydrothermal conditions. In addition, conventional nanoparticle growth generally results in larger particles at higher synthesis temperatures.[37,62,63] Therefore, the proximity of the final diameters of the MW-synthesized SnO_2 nanoparticles to that of the conventionally prepared SnO_2 is consistent with the notion that MW irradiation accelerated the growth of the resultant nanoparticles even at lower measured reaction temperatures (Table S1).

The plots illustrating the fits to the Avrami model for the conventional hydrothermal and the MW-assisted methods are shown in Fig. 5 and 6, respectively. The final MW-assisted synthesis condition was excluded for this portion of the analysis due to its lack of reaching an appreciable steady state temperature (Fig. S1). The fit windows for the various synthesis experiments were chosen such that they corresponded to the experimental isothermal conditions for subsequent Arrhenius analysis and the phase of nanoparticle growth past the initial incubation period in accordance with Avrami model assumptions.[56] The resultant fit parameters for the rate constant and Avrami exponents as well as the coefficient of determination, or R^2, values for all the presented fits are tabulated in Table S2.

To elucidate the potential origins of the observation of enhanced phase formation during MW-assisted synthesis of SnO_2, the Arrhenius parameters that relay the kinetic properties of a chemical reaction can be considered from the Arrhenius equation given by eqn (3):

$$k = A \exp\left(-\frac{E_a}{RT}\right) \tag{3}$$

where k is the reaction rate constant, A is the pre-exponential factor, E_a is the activation energy, R is the universal gas constant, and T is the absolute temperature. The equation can be algebraically rearranged such that a graphical plot of the

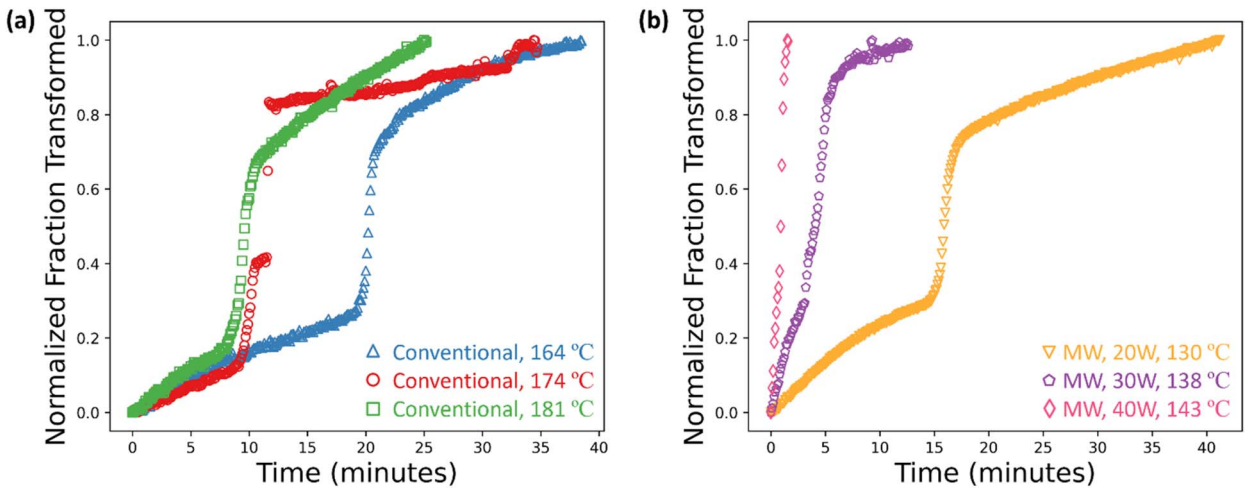

Fig. 4 Transformation curves derived from the PDF data during the SnO_2 nanoparticle synthesis experiments. (a) The evolution of the min—max normalized scale factors for the rutile SnO_2 phase from the conventional hydrothermal synthesis condition. (b) The evolution of the min—max normalized scale factors for the rutile SnO_2 phase from the MW-assisted synthesis condition.

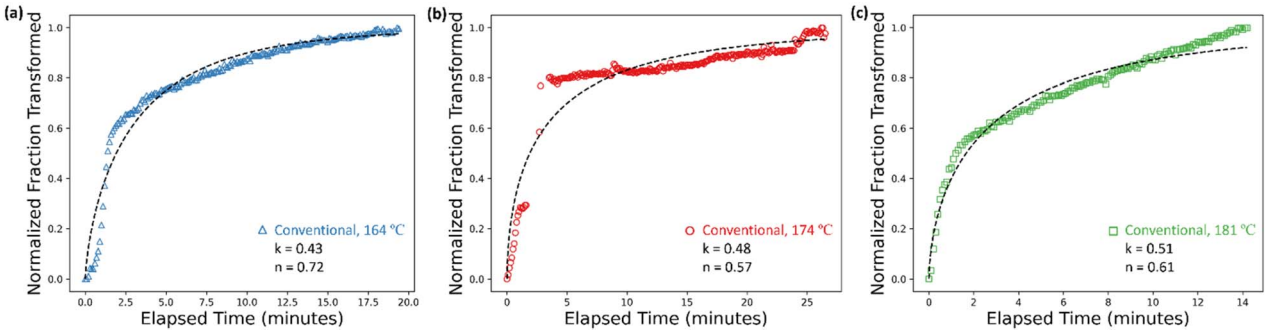

Fig. 5 The Avrami plots for the conventional hydrothermal synthesis conditions. The fitting was applied to the transformation curves following the first inflection point corresponding to the onset of the growth-dominated regime and when the reaction temperatures stabilized at the nominal temperatures at (a) 164 °C, (b) 174 °C, and (c) 181 °C. The respective rate constant, k, and Avarmi exponent, n, values are also shown.

natural logarithm of k as a function of the inverse T yields an Avrami plot in which the slope of the linear trend is related to the activation energy by $\frac{E_a}{R}$and the y-intercept of the plot is related to the pre-exponential factor by ln (A).

The Arrhenius plots constructed from the data for the conventional hydrothermal and MW-assisted synthesis methods for SnO_2 are shown in Fig. 7. The corresponding regression statistics are tabulated in Table S3. We note that the Arrhenius parameters are derived from experimentally accessible isothermal conditions with the present setup, with representative maximum temperatures recorded where steady-state temperatures weren't achieved. Accordingly, the values for the MW condition should be interpreted as comparative indicators and are used here to assess relative kinetic trends rather than absolute kinetic constants.

The resultant values for the apparent activation energy for the conventional synthesis and the MW-assisted synthesis methods are 16 kJ mol^{-1} and 270 kJ mol^{-1}, respectively. Interestingly, the apparent activation energy for the MW-assisted method is higher than that of the conventional hydrothermal reaction. This result deviates from many reports of reduced activation energies in MW processing, whether experimentally determined or ascribed to postulated mechanisms, relative to its conventional counterparts. However, given the number of experimental data points, it is not unreasonable to assume that the differences in the activation energies between the synthesis modalities in the present experimental conditions could be negligible. This would suggest that the reaction pathway for the irradiated synthesis is not meaningfully distinct from the conventional process. This is sensible in the present study given the relatively mild MW irradiation conditions. However, such a conclusion does not readily explain the observation of faster crystallization in the MW-synthesized SnO_2 nanoparticles.

On the other hand, the apparent pre-exponential factors determined for the conventional synthesis and the MW-assisted synthesis methods are 37 min^{-1} and 3.4 $\times 10^{34}$ min^{-1}, respectively, representing several magnitudes of increase for the pre-exponential term in the MW-irradiated process. Attributions to an increased pre-exponential factor accounting for improved reaction rates and/or yields in MW-assisted chemistry are not uncommon in the literature.[25–27,64] The experimental results in the present study further support prior findings which suggest that an effect of the applied MW field in MW-assisted chemistry

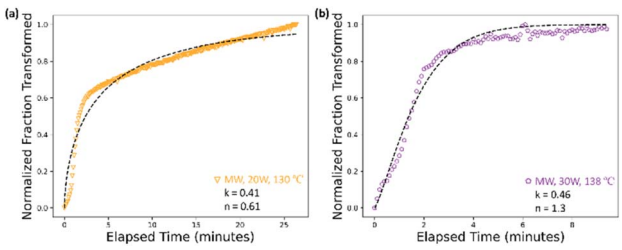

Fig. 6 The Avrami plots for the MW-assisted synthesis conditions. The fitting was applied to the transformation curves following the first inflection point corresponding to the onset of the growth-dominated regime and when the reaction temperatures stabilized at the nominal temperatures at (a) 130 °C and (b) 138 °C. The respective rate constant, k, and Avrami exponent, n, values are also shown.

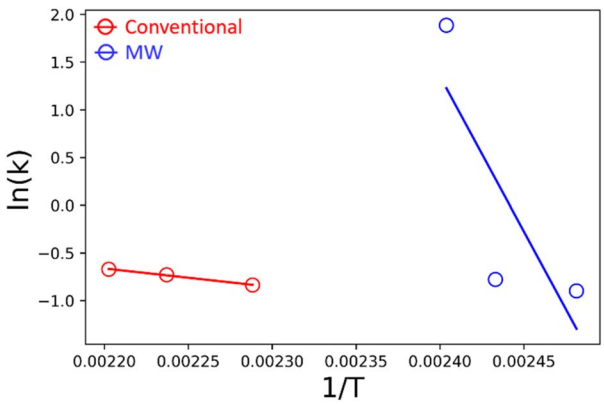

Fig. 7 The Arrhenius plots for the MW-assisted synthesis and conventional hydrothermal synthesis of SnO_2 nanoparticles. The E_a values for the conventional hydrothermal method and MW-assisted synthesis are 16 kJ mol^{-1} and 270 kJ mol^{-1}, respectively. The pre-exponential factors for the conventional hydrothermal method and the MW-assisted synthesis are 37 min^{-1} and 3.4 $\times$ 10^{34} min^{-1}, respectively.

is an increase in the corresponding pre-exponential factor rather than a decrease in the activation energy.

A common caveat in attributions to a nonthermal effect of the MW field in experimental studies is the matter of accurate temperature measurements. Indeed, the experimental difficulties of measuring the local, representative temperature in MW-assisted reactions remains an ongoing effort. Although the presented temperature measurements herein incorporated fiber optic probes as close to the reaction site as experimentally permissible, errors in representing the exact reaction temperature are expected. One way to estimate the extent of erroneous temperature measurements is through the substitution of the values for the conventional Arrhenius parameters into eqn (3) to calculate the corresponding temperatures under standard hydrothermal synthesis that could plausibly account for the rate constants observed during the MW-assisted reactions. Doing so for the experiments that reached steady state for comparison yields temperatures of 158 °C and 169 °C for the first and second MW conditions, respectively, representing an inaccuracy of 28 °C and 31 °C in the measured temperatures, respectively. Variations of this magnitude are modest and well within the realm of temperature gradients expected in MW processing,[65–67] initially suggesting that the experimental outcomes could simply stem from purely thermal phenomena albeit under MW irradiation. However, this does not fully represent the possibilities responsible for the faster crystallization rates shown in Fig. 4 under MW irradiation relative to conventional hydrothermal synthesis at the nominal temperatures determined *via* eqn (3).

One possible explanation involves the challenge of capturing the representative temperature in MW heating, *i.e.*, a disparity between the local reaction temperature and the measured bulk temperature. The observed rupture of the reaction vessel at the end of the second MW synthesis suggests that the reaction temperature may have exceeded the measured temperature. However, vessel failure alone does not confirm that the reaction volume experienced uniformly elevated temperatures. Localized heating, transient temperature gradients, or pressure pulses could have mechanically stressed the vessel walls or interfaces, leading to structural failure.

The phenomena of selective heating or "hot spots" is well documented within MW processing,[3,68] and reports of unique effects of MW processing have been linked to such characteristic behavior, even at the atomic scale.[7,36,69] Further experimental probes, such as high temporal and spatial thermal imaging or temperature-dependent chemical markers, would be necessary to better understand the correlation between local and bulk temperatures in MW-assisted reactions.[7,70,71] Nonetheless, localized temperatures or phenomena that aren't represented by the measured bulk temperatures could account for the notable crystallization rates observed in the MW experiments.

Conversely, if we consider that the measured temperatures adequately represented the bulk reaction environment in the compact vessel-probe setup, then the temperatures estimated from the Arrhenius relation still yielded lower values for the MW-irradiated reactions compared to the conventional syntheses, yet the former exhibited faster crystallization rates. This discrepancy suggests an additional influence of the MW field that is not fully described by a single thermally activated process.

In this case, findings of an increased pre-exponential factor with MW-assisted synthesis signify increases in the frequency of molecular collisions with the appropriate orientation and energy for the progression of a reaction. It is well known that MW radiation can induce molecular motion in the form of dielectric heating mechanisms, such as ionic conduction or dipolar rotation, in which charged particles oscillate due to the imposed alternating field.[72,73] Accordingly, MW coupling to polar solutes in the reaction could augment molecular motion in a manner that enhances solute collisions and overall reaction probability.[74] However, rather than simply an increase in the indiscriminate molecular motion typical of conventional thermal agitation, the influence of the MW field could induce steric effects through dipole alignment, thereby improving accessibility to reactive sites and further enhancing solute reactivity.[26,64] In other words, it is a specific molecular motion rendered by MW irradiation rather than a sole increase in the average molecular motion represented by an increased pre-exponential factor that is responsible for the reaction enhancements observed with MW-assisted synthesis. The polarity or polarizability of the irradiated species could also amplify such effects. It is well known that polar materials are highly efficient MW absorbers and therefore more susceptible to MW heating and its consequent effects.[75,76] The high electronegativity of the Cl and O atoms relative to the Sn species in the present experimental system can result in polar Sn–Cl and Sn–O bonds in the chemical system, leading to enhanced field-driven effects such as dipole reorientation or local heating.

The finding of an increased Arrhenius pre-exponential term in the present study invites further discussion into the contributing factors governing this term. The pre-exponential factor can be expressed in the general form by eqn (4):

$$A = \gamma\lambda^2\Gamma \tag{4}$$

where γ is a geometric factor representing the nearest-neighbor jump sites, λ is the jump distance between atoms, and Γ is the jump frequency. An initial inspection within the context of the MW effect typically rules out the jump frequency due to its value for that of atoms (10^{13} Hz) to be orders of magnitude higher than typical MW frequencies (*ca.* 10^9 Hz), making resonance between the two unlikely.[77] Although the number of jump sites and the jump distance have previously been cited to be constant for a given material, recent studies have challenged the assumption that these terms are immutable. The number of jump sites can be modified by point defects, such as lattice vacancies or interstitials, that could stem from an externally applied MW field.[30,48,78] The increasing variations in the short-range domain of the PDFs for the MW-assisted synthesis conditions illustrated by Fig. 3(c) could be indicative of atomic defects or local asymmetries encountered in the present study. Indeed, prior studies in field-assisted processing of metal oxides have attributed observations of abnormal structural

alterations and phase formation with the generation of defects.[6,10,79] Computational investigations have also postulated that oxygen point defects in oxide systems could impact phase stability and mediate phase transitions.[52,80,81] In a similar vein, the jump distance might also be affected by a proliferation of point defects that could subsequently distort the lattice structure. For example, prior *in-situ* studies of field-assisted processing techniques, including MW-assisted synthesis, have demonstrated anomalous behaviors in regard to lattice expansion in a variety of oxide systems.[30,79,82,83] The experimental outcomes involving abnormally large and/or anisotropic lattice expansion were not readily explainable by usual thermal expansion and instead attributed to a buildup of point defects, suggesting that externally applied fields can affect the collocation of lattice planes through defect formation. Taken altogether, these findings align with the concept that MW-assisted synthesis can plausibly influence chemical kinetics and reactivity *via* modifications to the pre-exponential factor.

4 Conclusions

This study submits experimental evidence that the faster crystallization of SnO_2 nanoparticles under MW-assisted hydrothermal synthesis originates from an elevated pre-exponential factor, rather than a reduced activation energy commonly credited in MW-assisted chemistry. The increased Arrhenius pre-exponential term reflects a higher frequency of successful molecular collisions for the initiation of a reaction that could stem from enhanced dipole alignment, solute mobility, or defect formation under the applied alternating MW field. By combining *in-situ* X-ray PDF analysis in conjunction with Avrami modelling and Arrhenius analysis, this work provides further clarity on the role of the MW field in chemical reactivity and materials synthesis. Further applications of advanced *in situ* probes or experimental systems to resolve the local temperature will be instrumental to unambiguously assess the nature and contributions of nonthermal MW effects. Complementary diagnostics to directly monitor or subsequently survey the atomic environment can also further link macroscale behavior to underlying atomic mechanisms. Nevertheless, the workflow demonstrated herein can be adapted to other material systems to gain a richer understanding of the mechanistic influences underlying MW-assisted synthesis.

Author contributions

Morgan Chen: investigation, formal analysis, writing – original draft, writing – review & editing. Laura Glei Graversen – formal analysis, writing – review & editing. Sanjit Ghose – resources, supervision. Kirsten M. Ø. Jensen – supervision. B. Reeja-Jayan – funding acquisition, supervision, writing – review & editing.

Conflicts of interest

There are no conflicts of interest to declare.

Data availability

The data supporting this article have been included as part of the supplementary information (SI). Supplementary information is available. See DOI: https://doi.org/10.1039/d5ta10373h.

Acknowledgements

This material is based upon work supported by the National Science Foundation Graduate Research Fellowship Program under Grant No. DGE2140739. Any opinions, findings, and conclusions or recommendations expressed in this material are those of the author(s) and do not necessarily reflect the views of the National Science Foundation. This research also used resources at the 28-ID-2 XPD beamline of the National Synchrotron Light Source II, a U.S. DOE Office of Science User Facility operated for the DOE Office of Science by Brookhaven National Laboratory under Contract No. DESC0012704. In addition, the authors would like to acknowledge the technical support of John Trunk of Brookhaven National Laboratory throughout the beamline experiments.

Notes and references

1 B. Reeja-Jayan and J. Luo, *MRS Bull.*, 2021, **46**, 26–35.
2 C. O. Kappe, *Angew. Chem., Int. Ed.*, 2004, **43**, 6250–6284.
3 H. J. Kitchen, S. R. Vallance, J. L. Kennedy, N. Tapia-Ruiz, L. Carassiti, A. Harrison, A. G. Whittaker, T. D. Drysdale, S. W. Kingman and D. H. Gregory, *Chem. Rev.*, 2014, **114**, 1170–1206.
4 S. Komarneni, Q. Li, K. M. Stefansson and R. Roy, *J. Mater. Res.*, 1993, **8**, 3176–3183.
5 G. A. Tompsett, W. C. Conner and K. S. Yngvesson, *Chem. Eur. J.*, 2006, **7**, 296–319.
6 N. Nakamura, L. Su, J. Bai, S. Ghose and B. Reeja-Jayan, *J. Mater. Chem. A*, 2020, **8**, 15909–15918.
7 A. Ramirez, J. L. Hueso, M. Abian, M. U. Alzueta, R. Mallada and J. Santamaria, *Sci. Adv.*, 2019, **5**, eaau9000.
8 H. Renuka, M. Chen, S. S. Kumar, L. Yang, M. T. Lanagan, S. Ghose and B. Reeja-Jayan, *Mater. Sci. Semicond. Process.*, 2025, **185**, 108966.
9 B. Reeja-Jayan, K. L. Harrison, K. Yang, C.-L. Wang, A. E. Yilmaz and A. Manthiram, *Sci. Rep.*, 2012, **2**, 1003.
10 N. Nakamura, M. W. Terban, S. J. L. Billinge and B. Reeja-Jayan, *J. Mater. Chem. A*, 2017, **5**, 18434–18441.
11 S. Saremi-Yarahmadi, B. Vaidhyanathan and K. G. U. Wijayantha, *Int. J. Hydrogen Energy*, 2010, **35**, 10155–10165.
12 A. Nozariasbmarz, K. Dsouza and D. Vashaee, *Appl. Phys. Lett.*, 2018, **112**, 093103.
13 R. Roy, Y. Fang, J. Cheng and D. K. Agrawal, *J. Am. Ceram. Soc.*, 2005, **88**, 1640–1642.
14 J. Cheng, R. Roy and D. Agrawal, *Mater. Res. Innovations*, 2002, **5**, 170–177.
15 O. C. Kappe, A. Stadler and D. Dallinger, *Microwaves in Organic and Medicinal Chemistry*, John Wiley & Sons, 2012, vol. 52.

16 C. O. Kappe, B. Pieber and D. Dallinger, *Angew. Chem., Int. Ed.*, 2013, **52**, 1088–1094.
17 J. Zhou, W. Xu, Z. You, Z. Wang, Y. Luo, L. Gao, C. Yin, R. Peng and L. Lan, *Sci. Rep.*, 2016, **6**, 25149.
18 M.-J. Zhang, Y. Duan, C. Yin, M. Li, H. Zhong, E. Dooryhee, K. Xu, F. Pan, F. Wang and J. Bai, *Sci. Adv.*, 2020, **6**, eabd9472.
19 Y. N. Chen, Z. J. Wang, T. Yang and Z. D. Zhang, *Acta Mater.*, 2014, **71**, 1–10.
20 Y.-J. Zhang, Z. J. Wang, Y. N. Chen and Z. D. Zhang, *J. Eur. Ceram. Soc.*, 2018, **38**, 105–111.
21 M. Zhou, L. Ai, L. Hong, C. Sun and Y. Yuan, *Metall. Mater. Trans. B*, 2023, **55**, 114–127.
22 M. A. Janney, H. D. Kimrey, W. R. Allen and J. O. Kiggans, *J. Mater. Sci.*, 1997, **32**, 1347–1355.
23 J. Fukushima, K. Kashimura, S. Takayama, M. Sato, S. Sano, Y. Hayashi and H. Takizawa, *Mater. Lett.*, 2013, **91**, 252–254.
24 V. Venkatachalam, B. Vaidhyanathan and J. Binner, *J. Eur. Ceram. Soc.*, 2020, **40**, 3974–3983.
25 J. G. P. Binner, N. A. Hassine and T. E. Cross, *J. Mater. Sci.*, 1995, **30**, 5389–5393.
26 M. Gharibeh, G. A. Tompsett, W. C. Conner and K. S. Yngvesson, *ChemPhysChem*, 2008, **9**, 2580–2591.
27 E. Haque, N. A. Khan, J. H. Park and S. H. Jhung, *Chem. - Eur. J.*, 2010, **16**, 1046–1052.
28 K. M. Ø. Jensen, C. Tyrsted, M. Bremholm and B. B. Iversen, *ChemSusChem*, 2014, **7**, 1594–1611.
29 G. R. Robb, A. Harrison and A. G. Whittaker, *PhysChemComm*, 2002, **5**, 135.
30 S. K. Jha, N. Nakamura, S. Zhang, L. Su, P. M. Smith, X. L. Phuah, H. Wang, H. Wang, J. S. Okasinski, A. J. H. McGaughey and B. Reeja-Jayan, *Adv. Eng. Mater.*, 2019, **21**, 1900762.
31 Q. Liu, M.-R. Gao, Y. Liu, J. S. Okasinski, Y. Ren and Y. Sun, *Nano Lett.*, 2016, **16**, 715–720.
32 S. J. L. Billinge and I. Levin, *Science*, 2007, **316**, 561–565.
33 T. L. Christiansen, S. R. Cooper and K. M. Ø. Jensen, *Nanoscale Adv.*, 2020, **2**, 2234–2254.
34 S. Tominaka, H. Yamada, S. Hiroi, S. I. Kawaguchi and K. Ohara, *ACS Omega*, 2018, **3**, 8874–8881.
35 H. Yamada, S. Tominaka, K. Ohara, Z. Liu, T. Okubo and T. Wakihara, *J. Phys. Chem. C*, 2019, **123**, 28419–28426.
36 F. Kishimoto, T. Yoshioka, R. Ishibashi, H. Yamada, K. Muraoka, H. Taniguchi, T. Wakihara and K. Takanabe, *Sci. Adv.*, 2023, **9**, eadi1744.
37 K. M. Ø. Jensen, M. Christensen, P. Juhas, C. Tyrsted, E. D. Bøjesen, N. Lock, S. J. L. Billinge and B. B. Iversen, *J. Am. Chem. Soc.*, 2012, **134**, 6785–6792.
38 M. Park, G. Wang, Y. Kang, D. Wexler, S. Dou and H. Liu, *Angew. Chem., Int. Ed.*, 2007, **46**, 750–753.
39 L. Jiang, G. Sun, Z. Zhou, S. Sun, Q. Wang, S. Yan, H. Li, J. Tian, J. Guo, B. Zhou and Q. Xin, *J. Phys. Chem. B*, 2005, **109**, 8774–8778.
40 Y. Liu, Y. Jiao, Z. Zhang, F. Qu, A. Umar and X. Wu, *ACS Appl. Mater. Interfaces*, 2014, **6**, 2174–2184.
41 P. J. Chupas, X. Qiu, J. C. Hanson, P. L. Lee, C. P. Grey and S. J. L. Billinge, *J. Appl. Crystallogr.*, 2003, **36**, 1342–1347.
42 P. Juhás, T. Davis, C. L. Farrow and S. J. L. Billinge, *J. Appl. Crystallogr.*, 2013, **46**, 560–566.
43 X. Yang, P. Juhas, C. L. Farrow and S. J. L. Billinge, *arXiv*, 2015, preprint arXiv:1402.3163, DOI: 10.48550/arXiv.1402.3163.
44 C. L. Farrow, P. Juhas, J. W. Liu, D. Bryndin, E. S. Božin, J. Bloch, T. Proffen and S. J. L. Billinge, *J. Phys.: Condens. Matter*, 2007, **19**, 335219.
45 Th. Proffen and S. J. L. Billinge, *J. Appl. Crystallogr.*, 1999, **32**, 572–575.
46 M. J. Taylor and J. M. Coddington, *Polyhedron*, 1992, **11**, 1531–1544.
47 A.-F. Shihada, A. S. Abushamleh and F. Weller, *Z. Anorg. Allg. Chem.*, 2004, **630**, 841–847.
48 N. Nakamura, L. Su, H. Wang, N. Bernstein, S. K. Jha, E. Culbertson, H. Wang, S. J. L. Billinge, C. S. Hellberg and B. Reeja-Jayan, *J. Mater. Chem. A*, 2021, **9**, 8425–8434.
49 B. Panzarella, G. A. Tompsett, K. S. Yngvesson and W. C. Conner, *J. Phys. Chem. B*, 2007, **111**, 12657–12667.
50 C. E. White, J. L. Provis, B. Bloomer, N. J. Henson and K. Page, *Phys. Chem. Chem. Phys.*, 2013, **15**, 8573.
51 M. E. Ayturk, E. A. Payzant, S. A. Speakman and Y. H. Ma, *J. Membr. Sci.*, 2008, **316**, 97–111.
52 F. Zhang, P. J. Chupas, S. L. A. Lui, J. C. Hanson, W. A. Caliebe, P. L. Lee and S.-W. Chan, *Chem. Mater.*, 2007, **19**, 3118–3126.
53 M. E. Potter, M. E. Light, D. J. M. Irving, A. E. Oakley, S. Chapman, P. Chater, G. Cutts, A. Watts, M. Wharmby, B. D. Vandegehuchte, M. W. Schreiber and R. Raja, *Phys. Chem. Chem. Phys.*, 2020, **22**, 18860–18867.
54 R. S. Christensen, M. Kløve, M. Roelsgaard, S. Sommer and B. B. Iversen, *Nanoscale*, 2021, **13**, 12711–12719.
55 J.-L. Mi, K. M. Ø. Jensen, C. Tyrsted, M. Bremholm and B. B. Iversen, *CrystEngComm*, 2015, **17**, 6868–6877.
56 K. Shirzad and C. Viney, *J. R. Soc., Interface*, 2023, **20**, 20230242.
57 S. M. Everett, C. J. Rawn, D. J. Keffer, D. L. Mull, E. A. Payzant and T. J. Phelps, *J. Phys. Chem. A*, 2013, **117**, 3593–3598.
58 J. R. Sonawane, S. Patil and A. A. Kulkarni, *Ind. Eng. Chem. Res.*, 2023, **62**, 14199–14211.
59 J. R. Eltzholtz, C. Tyrsted, K. M. Ø. Jensen, M. Bremholm, M. Christensen, J. Becker-Christensen and B. B. Iversen, *Nanoscale*, 2013, **5**, 2372.
60 P. Nørby, M. Roelsgaard, M. Søndergaard and B. B. Iversen, *Cryst. Growth Des.*, 2016, **16**, 834–841.
61 Y. Zhou, W. Lin, F. Yang, W. Fang, J. Huang and Q. Li, *Chem. Phys.*, 2014, **441**, 23–29.
62 H. Liu, H. Zhang, J. Wang and J. Wei, *Arab. J. Chem.*, 2020, **13**, 1011–1019.
63 C. Tyrsted, K. M. Ørnsbjerg Jensen, E. D. Bøjesen, N. Lock, M. Christensen, S. J. L. Billinge and B. Brummerstedt Iversen, *Angew. Chem., Int. Ed.*, 2012, **51**, 9030–9033.
64 M. R. Rosana, Y. Tao, A. E. Stiegman and G. B. Dudley, *Chem. Sci.*, 2012, **3**, 1240.
65 C. O. Kappe, *Chem. Soc. Rev.*, 2013, **42**, 4977.

66 B. García-Baños, J. J. Reinosa, F. L. Peñaranda-Foix, J. F. Fernández and J. M. Catalá-Civera, *Sci. Rep.*, 2019, **9**, 10809.
67 P. Boch, *Solid State Ionics*, 1997, **101–103**, 1229–1233.
68 B. Aman, S. Acharya and B. Reeja-Jayan, *Adv. Eng. Mater.*, 2024, **26**, 2302065.
69 I. Julian, H. Ramirez, J. L. Hueso, R. Mallada and J. Santamaria, *Chem. Eng. J.*, 2019, **377**, 119764.
70 Y. Tao, C. Teng, T. D. Musho, L. van de Burgt, E. Lochner, W. T. Heller, G. F. Strouse, G. B. Dudley and A. E. Stiegman, *J. Phys. Chem. B*, 2021, **125**, 2146–2156.
71 L. S. Gangurde, G. S. J. Sturm, T. J. Devadiga, A. I. Stankiewicz and G. D. Stefanidis, *Ind. Eng. Chem. Res.*, 2017, **56**, 13379–13391.
72 J. Sun, W. Wang and Q. Yue, *Materials*, 2016, **9**, 231.
73 D. E. Clark and W. H. Sutton, *Annu. Rev. Mater. Res.*, 1996, **26**, 299–331.
74 J. Jacob, L. H. L. Chia and F. Y. C. Boey, *J. Mater. Sci.*, 1995, **30**, 5321–5327.
75 A. M. Rodríguez, P. Prieto, A. de la Hoz, Á. Díaz-Ortiz, D. R. Martín and J. I. García, *ChemistryOpen*, 2015, **4**, 308–317.
76 C. Oliver Kappe, *Chem. Soc. Rev.*, 2008, **37**, 1127.
77 J. D. Katz, *Annu. Rev. Mater. Sci.*, 1992, **22**, 153–170.
78 Q. Chen, X. Luo, G. Mu, X. Mao, H. Yin, E. H. Lester and T. Wu, *ACS Sustain. Chem. Eng.*, 2024, **12**, 15134–15146.
79 J. -M. Lebrun, C. S. Hellberg, S. K. Jha, W. M. Kriven, A. Steveson, K. C. Seymour, N. Bernstein, S. C. Erwin and R. Raj, *J. Am. Ceram. Soc.*, 2017, **100**, 4965–4970.
80 M. Jongmanns and D. E. Wolf, *J. Am. Ceram. Soc.*, 2020, **103**, 589–596.
81 S. Fabris, *Acta Mater.*, 2002, **50**, 5171–5178.
82 E. K. Akdoğan, İ. Şavklıyıldız, H. Biçer, W. Paxton, F. Toksoy, Z. Zhong and T. Tsakalakos, *J. Appl. Phys.*, 2013, **113**, 233503.
83 S. K. Jha, H. Charalambous, H. Wang, X. L. Phuah, C. Mead, J. Okasinski, H. Wang and T. Tsakalakos, *Ceram. Int.*, 2018, **44**, 15362–15369.